JOURNAL OF GEOPHYSICAL RESEARCH, VOL. 113, D12117, doi:10.1029/2007JD009418, 2008

Incident spectral irradiance in the Arctic Basin during the summer and fall

Thomas C. Grenfell[1] and Donald K. Perovich[2]

Received 25 September 2007; revised 28 January 2008; accepted 12 March 2008; published 27 June 2008.

[1] Calibrated values of incident spectral irradiance are reported from the Healy Oden Transarctic Experiment during August and September 2005. Spectra were obtained for a wide range of solar zenith angles, cloud conditions, and surface types to provide basic data for regional shortwave radiative energy balance calculations as well as climate model parameterization and validation. Supervised principal component analysis on the spectral continuum showed that three principal components explain over 99% of the variance resulting from darkening across the solar spectrum with increasing cloud cover by volume scattering, from stronger attenuation in the solar infrared relative to visible wavelengths by H_2O, and from Rayleigh scattering. Comparison of the observations with the atmospheric radiation model SBDART showed that good agreement was obtained varying only the cloud optical depth. Applying the model, we showed how the surface albedo affects incident spectral irradiance under clear as well as cloudy skies, and we obtained a quantitative estimate of the visual effects of "water sky" and "ice blink." We also determined the spectral albedo of the atmosphere for a dense arctic stratus cloud deck decoupled from the influence of the underlying surface. Incident spectral irradiances were integrated numerically and compared with calibrated pyranometer observations. Agreement was within 5% for cases where the cloud transparency and incident irradiance did not fluctuate strongly over the 10-min pyranometer recording intervals. A new set of values for total albedo for clear versus cloudy conditions at high and low Sun angles is presented for six prominent arctic surface types.

Citation: Grenfell, T. C., and D. K. Perovich (2008), Incident spectral irradiance in the Arctic Basin during the summer and fall, *J. Geophys. Res.*, *113*, D12117, doi:10.1029/2007JD009418.

1. Introduction

[2] Total incident solar irradiance values at the surface integrated over the solar spectrum (300–3000 nm), and corresponding total albedos abound from almost all experimental research stations and field experiments in the Arctic regions. These values are obtained with shortwave pyranometers and are used to provide fundamental input for studying the interaction of solar radiation with the surface and atmosphere in the Arctic. Values of total incident irradiance (F_o), albedo (α_{tot}), and extinction coefficient (K_{tot}), however, are not sufficient in themselves for detailed modeling over snow and ice surfaces either on local, regional, or basin-wide scales. Although considerable information is available about the spatial and temporal distribution of total albedo and related snow properties [*Radionov et al.*, 1996], values of incident spectral irradiance [$F_o(\lambda)$] are needed because of the strong wavelength variations in both the ambient radiation field and the optical properties of the underlying ice and snow [*Sauberer*, 1950; *Grenfell and Maykut*, 1977, hereinafter referred to as GM77; *Grenfell and Perovich*, 1981; *Perovich and Govoni*, 1991; *Warren*, 1984; *Brandt and Warren*, 1993; *Warren et al.*, 2006]. The spectral albedo of tundra in the Arctic coastal regions also has a strong wavelength dependence [*Grenfell and Perovich*, 1984, 2004].

[3] Of strong current interest for regional energy balance models of the polar regions as well as global climate models (GCM) [GM77; *Briegleb and Light*, 2007; *Alexandrov et al.*, 2004; *Holland and Bitz*, 2003; *Holland et al.*, 2006] are a set of radiative processes that produce "ice-albedo feedback," which has profound consequences for large-scale trends in sea ice concentration. To specify the solar radiative energy absorption and total albedo for a given sea ice type using wavelength-integrated irradiance data, formulae of the following types can be used (see, e.g., GM77):

$$\alpha_{tot} = \frac{\sum_j \int_{\Delta\lambda_j} \alpha_\lambda \cdot F_o(\lambda)\, d\lambda}{\sum_j \int_{\Delta\lambda_j} F_o(\lambda)\, d\lambda} \quad (1)$$

[1]Department of Atmospheric Sciences, University of Washington, Seattle, Washington, USA.
[2]ERDC-CRREL, Hanover, New Hampshire, USA.

0148-0227/08/2007JD009418$09.00

$$K_{\mathrm{tot}} = \frac{\sum_{\mathrm{j}} \int_{\Delta\lambda_{\mathrm{j}}} K_\lambda \cdot F_{\mathrm{net}}(\lambda, z)\, d\lambda}{\sum_{\mathrm{j}} \int_{\Delta\lambda_{\mathrm{j}}} F_{\mathrm{net}}(\lambda, z)\, d\lambda} \quad (2)$$

$$I_{\mathrm{o}} = \frac{\sum_{\mathrm{j}} \int_{\Delta\lambda_{\mathrm{j}}} F_{\mathrm{net}}(\lambda, z_{\mathrm{ref}})\, d\lambda}{\sum_{\mathrm{j}} \int_{\Delta\lambda_{\mathrm{j}}} (1-\alpha_\lambda) \cdot F_{\mathrm{o}}(\lambda)\, d\lambda}. \quad (3)$$

[4] In the above, K_λ is the asymptotic spectral extinction coefficient, $F_{\mathrm{net}}(\lambda, z)$ is the net spectral irradiance at depth z in the ice, z_{ref} is a reference depth near 0.1 m, chosen to include the zone where the direct incident irradiance is diffused and most of the solar infrared absorbed. The quantity I_{o} (e.g., GM77) is the fraction of net irradiance reaching a reference depth, z_{ref}, in the ice and is used to parameterize shortwave energy absorption within the ice taking into account the radiation extinction in the near-surface layers where the bulk attenuation is poorly represented by an exponential decrease. These formulae, or any more general treatment of radiative interaction processes and sea ice extent, clearly require a detailed knowledge of $F_{\mathrm{o}}(\lambda)$. For each of the above equations, the integral domain spans the full shortwave (SW) spectrum, but it is represented as being broken up into a finite sum over individual wavelength bands, $\Delta\lambda_{\mathrm{j}}$, a representation presently used to streamline calculations in complex climatological models [*Curry et al.*, 1995, 2001].

[5] A recently proposed upgrade to the sea ice component of the Community Climate System Model [*Briegleb and Light*, 2007] uses three separate bands depending on ice type. Unless otherwise stated, we use a single term in the summation and a single $\Delta\lambda$ that spans the entire shortwave spectrum. To calculate regional values, area-weighted averages over individual ice types are required. Because α_λ and K_λ depend on ice type and in some cases on location, an investigation of such averages is beyond the scope of the present work.

[6] The need for accurate values of $F_{\mathrm{o}}(\lambda)$ is clear; however, the spectral dependence is of central importance. Because of the appearance of $F_{\mathrm{o}}(\lambda)$ or $F_{\mathrm{net}}(\lambda, z)$ in both the numerator and denominator in the above equations, the quantities in equations (1) through (3) are not sensitive to the absolute values of $F_{\mathrm{o}}(\lambda)$. The use of equations (1) through (3) makes it possible to address the calculation of the radiative energy balance in two distinct steps: (1) determination of the spectral dependence, which is in general much more reliable than a full absolute calibration, followed by (2) the complete calibration. The latter is traditionally difficult, but it can be checked against pyranometer readings for an estimate of the accuracy. In general, step 1 is much less sensitive to problems associated with absolute calibration.

[7] Both the magnitude and spectral dependence of $F_{\mathrm{o}}(\lambda)$ depend most strongly on the cloud cover, primarily due to the effects of atmospheric water vapor and cloud particulates in both solid and liquid forms, and the solar zenith angle (θ_{o}). The cloud cover in the Arctic is typically optically thinner compared with lower latitudes and the predominant cloud types differ as well [GM77; *Warren et al.*, 2007; *Hahn et al.*, 2001]. Complete overcast conditions including a well developed stratus layer are common, particularly in the summer months when the incident shortwave radiation is strongest. The solar zenith angle is also large so that small changes in θ_{o} have a strong influence on $F_{\mathrm{o}}(\lambda)$ at all wavelengths. Other atmospheric gasses and aerosols can also have an effect, but the influence of variations in the concentrations of these components are generally much less and are typically of interest over limited wavelength ranges.

2. Previous Results

[8] Initial studies investigating the importance of the spectral dependence of F_{o} on the influence of the radiation incident upon sea ice (GM77) made use of clear-sky results for an air mass of 2 [solar zenith angle of 60°] at midlatitudes [*Gast*, 1960] and a cloudy sky spectrum from *Sauberer and Dirmhirn* [1958]. The cloudy spectrum had actually been measured in the Austrian Alps and had a relatively low precision. It provided an overestimate of cloud attenuation for Arctic conditions, but it was the only spectrum available at the time. The results of *Gast* [1960] are of high precision but also apply to midlatitude atmospheric condition and over represent the water vapor content of the Arctic atmosphere. The study did, however, show the significance of selective absorption of red and infrared radiation by a cloud cover. This causes an increase in α_{tot} and a decrease in K_{tot} for cloudy conditions because of the preferential decrease in the red and infrared weighting contributions in equations (1) and (2).

[9] *Grenfell and Perovich* [1984] used a calibrated quartz-halogen lamp to attempt to determine direct observational values at Barrow, Alaska; however, they had a problem with the power supply for the lamp, which was apparently run at too high power, and the resulting incident spectra were distorted. That study did show the effects of a variety of Arctic cloud conditions. *Grenfell* [1991] introduced a correction to $F_{\mathrm{o}}(\lambda)$ to provide better consistency with the clear-sky results of *Gast* [1960], but those estimates were still more characteristic of water vapor amounts found at mid latitudes. The spectra were also limited in spectral resolution. *Grenfell and Perovich* [2004] used much more realistic incident spectra with greatly improved spectral resolution for both clear and full overcast conditions; however, those values were obtained in the Antarctic summer seasonal sea ice zone. This case was from a polar marine environment with melting sea ice at the surface and came much closer to matching the Arctic than previous estimates, but only the two extremes were reported, clear and full heavy overcast conditions. Actual Arctic observations are thus still needed.

[10] *Rabbette and Pilewskie* [2002] have reported averaged incident spectra from May and June 1998 obtained during the SHEBA experiment. They carried out a detailed principal component analysis on the full spectral data set. Their results will be compared below with a similar analysis based on the present data set.

3. Field Program and Instrumentation

[11] Observations of incident irradiance were carried out during the Healy Oden Trans-Arctic Expedition (HOTRAX)

Figure 1. Track of U.S. Coast Guard Cutter *Healy* during the Healy Oden Trans-Arctic Expedition (HOTRAX) Arctic Basin traverse. The incident spectral irradiance observation sites are indicated by the circles. Data were taken from 7 August through 26 September, beginning in the Beaufort Sea proceeding across the pole and ending just northeast of Svalbard.

traverse of the Arctic Basin in August–September 2005 on the U.S. Coast Guard Cutter *Healy*. A map of the ship's track together with the incident spectral irradiance measurement sites is shown in Figure 1. The spectral incident solar irradiance was measured on 42 occasions using an Analytical Spectral Devices (ASD) FieldSpec Pro Spectroradiometer. The instrument provided spectral coverage from 350 to 2500 nm with a spectral resolution of 3 to 10 nm in the UV/visible and solar IR, respectively. Measurements were made near solar noon from the roof of the bridge of the ship. The location was chosen to minimize the effects of shadowing of the incident solar radiation by the ship's superstructure.

[12] Immediately before every set of observations, we measured the spectrum of a calibration lamp in the laboratory to determine the instrument sensitivity. The irradiance calibration was carried out using an Oriel stabilized power supply with a calibrated quartz halogen lamp running at 7.90 A and 120.0 V. The lamp was mounted in an aluminum case designed for field operation with a set of four progressive baffles along the light path to isolate the direct beam and remove stray light. In preparation for each set of observations, the calibration lamp was warmed up for approximately 15 min so it could reach thermal equilibrium. The irradiance probe, connected by an optical fiber to the spectrophotometer, was then exposed to the beam and the integration time for the ASD was set using the standard software provided by the manufacturer. The probe was located at a distance from the lamp of approximately 54 cm rather than the standard 50 cm, and the standard irradiance values were adjusted using the $1/r^2$ law. The instrument was then carried outside and the incident irradiance measurements taken. Each measurement took about 10 s during which 40 scans were recorded and averaged together during subsequent data processing. On occasion, the sensitivity of the instrument readjusted itself during the observation interval, and the affected data set was discarded.

[13] To measure spectral irradiance we fitted the spectroradiometer with an irradiance receptor we constructed in our machine shop at the University of Washington. The receptor consists of a Spectralon® diffuser mounted on a black-anodized plate with an optical fiber mounted on a "gooseneck" arm as shown in Figure 2 designed to accommodate the standard ASD optical fiber. The receptor was attached to an aluminum arm so that it could be extended away from the observer holding the instrument, minimizing the shadowing effect. A bubble level was mounted on the arm to allow us to insure that the plate was held horizontal for each observation. For optimal performance the receptor arm was pointed toward the Sun to avoid shadowing by the fiber mount, although the accuracy was preserved as long as the solar azimuth relative to the arm was less than 90°. Shadowing of the diffuse component of the radiation by the fiber mount, the observer, and other obstacles in the field of view was taken into account as described below.

[14] To ensure accurate results, particularly at low-Sun angle under clear conditions, the directional sensitivity of the irradiance receptor must also be taken into account. A series of tests was carried out in the laboratory prior to the field experiment by illuminating the receptor with a collimated beam over a range of incidence angles from 0 to 90°.

Figure 2. University of Washington irradiance receptor adapted for use with the Analytical Spectral Devices (ASD) standard broadband optical fiber.

The beam illuminated the Spectralon plate uniformly, and care was taken to align the axis of rotation of the beam with the surface of the plate. The stray diffuse light component was removed by assuming this component contributed the entire reading at 90° and that the diffuse light was uniform. The diffuse component was found to be less than 0.009 of the reading at 0°. All intensities were normalized to 1.0 at 0° for direct comparison with an ideal cos(Θ) dependence needed to measure irradiance directly. The calibration was carried out on three separate occasions and the results averaged to give the curves shown in Figure 3. The calibration was done using a different spectrophotometer whose spectral range was limited to 320 to 1100 nm, and the results shown are averages over that spectral range; however, the reflectance specifications for Spectralon are uniform from the near UV into the solar infrared to at least 2500 nm. We noticed no significant spectral dependence during the calibration, so we have assumed that the present results apply to the full spectral range of the ASD spectrophotometer. The receptor sensitivity is very close to that of the ideal cosine response, and the error was measured at 2% or less for all angles except the point at 75° (+4%). The error bars in Figure 3a denote the standard deviation of the observations, and all the points lie on the cosine curve within the limits of experimental uncertainty. Consequently, we have assumed that the cosine error can be neglected.

4. Observational Data

[15] Observations were taken almost every day near solar noon from 7 August to 26 September throughout the traverse. Cloudy conditions were encountered in 85% of the cases, with 40% of these cloudy enough that the solar disk was not visible. Conditions with the solar disk unobscured by clouds were recorded about 15% of the time with clear skies only 6% of the time. These proportions are generally consistent with statistics compiled from the Soviet and Russian NP drifting stations [*Alexandrov et al.*, 2004] although our statistical sample is much smaller.

[16] The measurement location on the flying bridge of the ship was above most, but not all, of the ship's structure. To correct the observation of the diffuse incident component for shadowing by the superstructure, the observer, and the optical fiber mount on the receptor, a shadowing correction was applied assuming that the diffuse radiation was isotropic. The irradiance integral at the detector over solid angle, Ω, in the upward hemisphere,

$$\left[\int_{2\pi} \mathrm{I}_{\mathrm{down}}(\Omega)\cdot\cos(\theta)\cdot d\Omega\right],$$

was evaluated taking into account the angular extent and direction of all obstacles in the field of view. A given object was assumed to be either rectangular or spherical. The

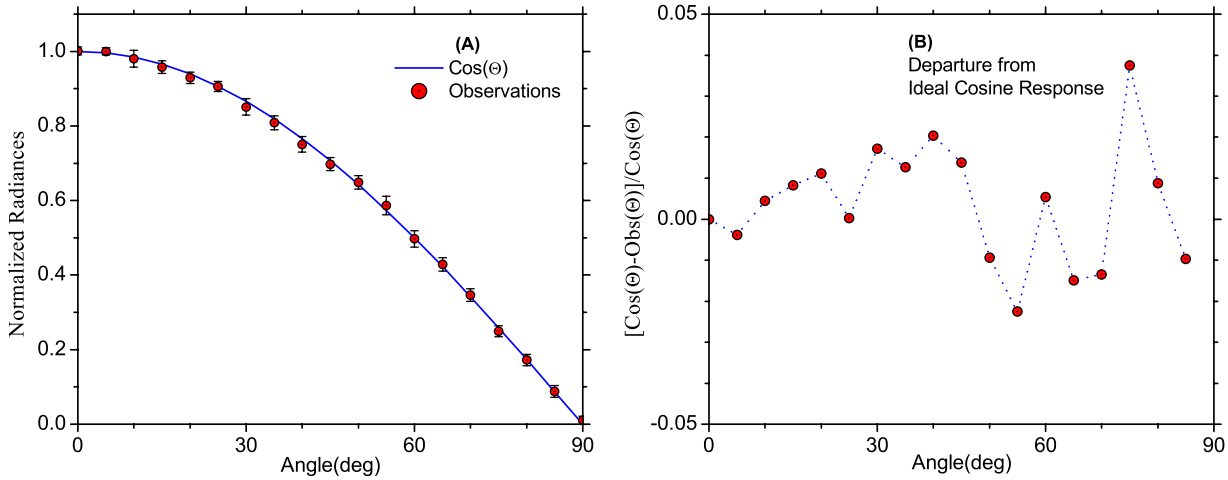

Figure 3. Calibration of the irradiance receptor: (a) relative sensitivity versus incidence angle of beam on the detector, Θ and (b) fractional departure from ideal cosine response.

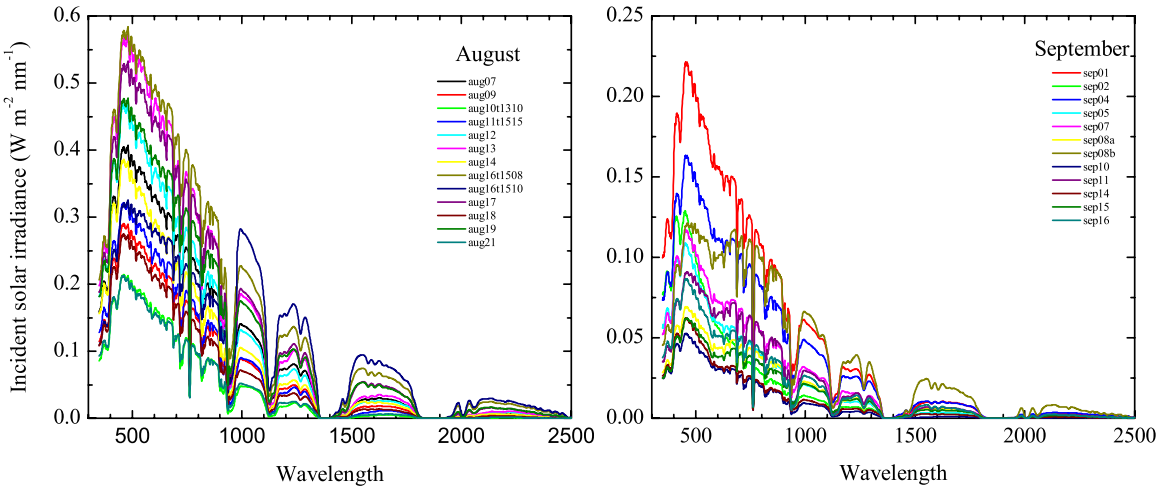

Figure 4. Observed spectra for all days during the transect: (left) August and (right) September.

reflectance of black surfaces such as the ship's superstructure was assumed to be zero, and the reflectance of the white objects, such as antenna domes, were assumed to be 0.7. The observers usually wore dark clothing, also assumed to be black. The total diffuse shadowing correction for bridge-based observations at the ship's rail was found to be 4.1%.

[17] Observations were obtained for a wide range of cloud conditions and solar zenith angles. Figure 4 shows the full range for August (left) and September (right). The general decrease in light levels with solar elevation during the two months is apparent. This overall trend was modulated by changes in the location of the ship, particularly the latitude, as well as cloud cover, local ice concentration, and changes in the atmospheric temperature and humidity profiles. Although we do not have sufficient data to investigate all these effects in detail, we isolate the dominant direct effects such as solar elevation, cloudiness and underlying surface type by making use of the observational data supplemented by theoretical model calculations.

4.1. Clear Skies

[18] Observations from the clearest sky cases are shown in Figure 5. In all these cases the solar disk was clearly visible, but in August the sky was never totally clear during the observation time interval near solar noon. In September, the cloud cover decreased somewhat providing four cloud-free cases. In Figure 5 we also indicate the presence and the wavelengths of the major solar and terrestrial absorption features. These occur at the expected wavelengths, as listed in the Figure 5 caption.

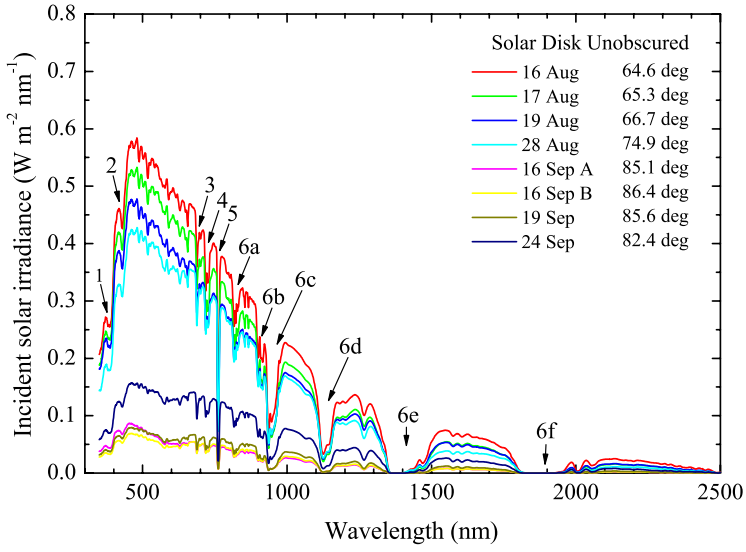

Figure 5. Spectra for cases for which the solar disk was clearly visible in August and for clear skies in September with low-Sun angle. The legend shows the date and solar zenith angle for each spectrum. The following atomic and molecular absorption features are clearly present: 1, Ca II H/K, 393–6 nm; 2, Fe/Ca, 431 nm; 3, O_2 B, 686–8 nm; 4, H_2O, 718–29; 5, O_2 A, 759–65; 6a, H_2O, 820 nm; 6b, H_2O, 910 nm; 6c, H_2O, 933–46 nm, 6d, H_2O, 1118–44 nm, 6e, H_2O, 1350–1480 nm; and 6f, H_2O, 1810–1950 nm.

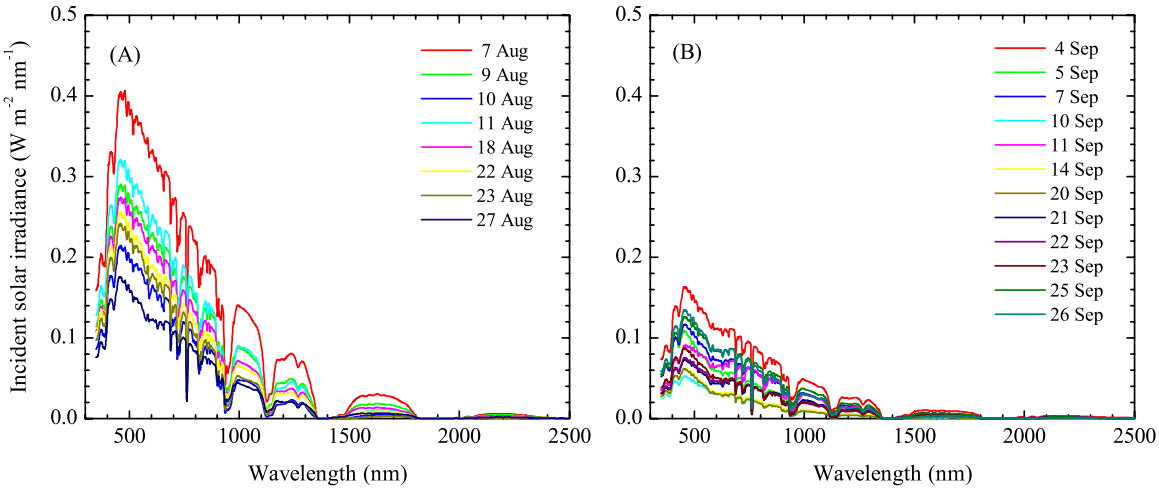

Figure 6. Complete overcast observations, with solar disk not visible for (a) August and (b) September.

[19] Note the appearance of an apparent broad absorption feature for low-Sun angle centered at about 600 nm. Concerns about instrument stability suggested this might be a problem with the optimization, but this was not the case. It is an enhancement of the Chappuis band of ozone seen in the spectra for higher Sun angle due to the increased atmospheric path length together with flattening of the spectrum in the blue and near ultraviolet by the strong wavelength dependence of Rayleigh scattering.

4.2. Complete Overcast

[20] Observations under conditions of complete overcast and uniform stratus cloud cover were common as is characteristic for summer conditions over Arctic sea ice. The spectra for those cases are shown in Figure 6. The series is dominated by the decrease due to the seasonal increase in solar zenith angle over the 2-month period, and there are significant differences between the clear and cloudy cases. A detailed discussion of these effects is deferred until a later section in order to show corresponding modeling results.

5. Principal Component Analysis

[21] To investigate significant variational patterns in the observed data, a principal component (*PC*) analysis was carried out using the software program Mathcad. To avoid the bias due to the far more frequent occurrence of cloudy conditions, a supervised analysis was performed. A total of eight cases were selected spanning a range of solar zenith angles from 65° to 86° for clear versus cloudy sky conditions. Eleven wavelengths from 350 to 2140 nm were selected to represent the spectral shape of the continuum avoiding the major absorption bands. Further, to avoid the bias due to large differences in irradiance at different wavelengths, we normalized all spectra to a reference spectrum. The eigenvectors of the first three principal components are shown in Figure 7

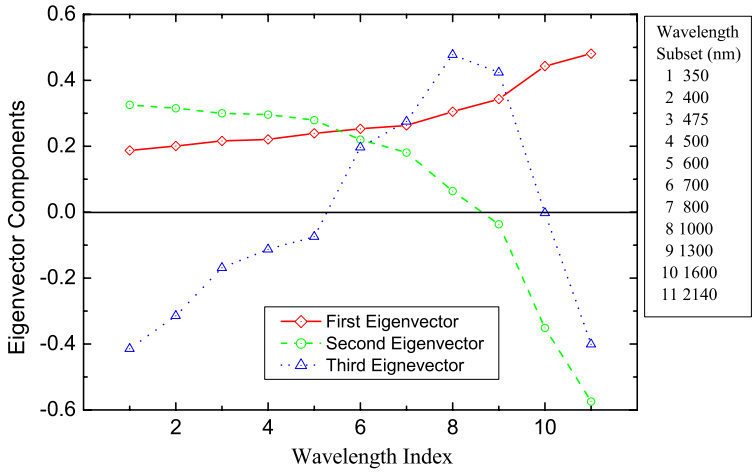

Figure 7. Principal component analysis results showing the first three eigenvectors, *PC*1, *PC*2, and *PC*3. The corresponding eigenvalues, representing the fraction of explained variance, are 0.948, 0.047, and 0.004, respectively. The set of wavelengths included in the analysis is given in the box to the right of the plot.

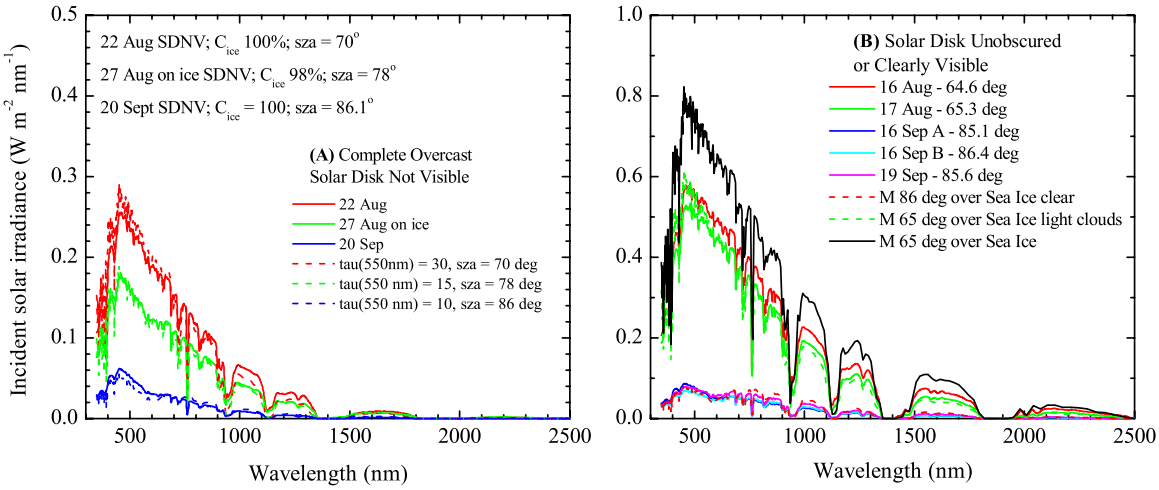

Figure 8. Comparison of observations (solid lines) with SBDART model results (dashed lines and solid black line) using the standard sub-Arctic atmosphere for summer and early fall: (a) complete overcast, with solar disk not visible at solar zenith angles (θ_o) of 70°, 78°, and 86° and τ_{cloud} values of 30, 15, and 10, respectively, and (b) solar disk unobscured or clearly visible, with $\theta_o = 65°$ and $\tau_{cloud} = 0$ and 5 and $\theta_o = 86°$ and $\tau_{cloud} = 0$. C_{ice} is sea ice concentration, and sza is the solar zenith angle.

together with a list of the selected wavelengths. The first principal component, *PC*1, explains 94.8% of the total variance, and over 99.9% of the variance in the data set is explained by the first three components.

[22] *PC*1 represents a covariational mode associated with general attenuation due to extinction at all wavelengths resulting from the addition of a cloud cover. The attenuation increases from a minimum at 350 nm to a maximum at 2140 nm dominated by volume scattering by cloud particles. The larger variation in the infrared is a component from the increased absorption by H_2O at longer wavelengths. In effect, it is an in-phase variation component. *PC*2, represents a spectral gradient mode and represents most of the effect of preferential absorption in the solar infrared due to the H_2O associated with the clouds. It represents the residual decrease at wavelengths greater than 1000 nm contrasted with the relative increase at short wavelengths unexplained by *PC*1. Both *PC*1 and *PC*2 are affected by the general attenuation by the clouds as well as the preferential absorption in the infrared. *PC*3 is a bending mode, a relative decrease across the visible and into the ultraviolet as well as a residual decrease at the longest wavelengths 1600 nm and 2140 nm. It has a contribution from the influence of Rayleigh scattering, and it includes the accentuation of the Chappuis band for large solar zenith angles. Since *PC*3 explains only about 0.5% of the variance, however, it may also include a contribution from random error.

[23] The principle components of *Rabbette and Pilewskie* [2002] differ from ours in that they include the entire spectrum in the analysis rather than taking a subset of wavelengths designed to isolate the continuum. As a result, the variance associated with low signal-to-noise ratios in the near infrared H_2O bands shows up strongly in their *PC*2, *PC*3 and *PC*4 eigenvectors. Their normalization also differs somewhat from ours. Despite this, the two sets of *PC*1 and *PC*2 vectors are very similar in character, theirs also indicating an in-phase intensity variation and a spectral gradient variation. Inclusion of the full spectra including the strong absorption bands introduces more independent variations, and their analysis requires 5 components to explain 99% of the variance for the complete downwelling spectra.

6. Comparison With Atmospheric Radiative Transfer Model

[24] To calculate model values of $F_o(\lambda)$, we used the radiative transfer code SBDART [*Ricchiazzi et al.*, 1998], a plane parallel atmospheric radiation model for clear and cloudy conditions based on the radiative transfer kernel DISORT. The calculations below consist of a 24-stream model using the standard sub arctic summer atmosphere included in the computer code. The wavelength range spanned 350 to 2500 nm, and the spectral resolution was chosen to increase smoothly from 1 nm at 350 nm to 5 nm at 2500 nm. This resolution was slightly greater than for the observed incident spectra. The albedos for the underlying surface were specified using recent surface-based field observations [*Perovich et al.*, 2002; *Grenfell and Perovich*, 2004]. This combination was used to represent summer and fall conditions in the Arctic. For cloudy cases we used a single cloud layer extending from 1000 to 5000 m above the surface with optical depths varied to fit the different cases. The values of solar zenith angle were determined from the ship's position and time of day from a standard ephemeris. Although SBDART is extremely flexible in describing the characteristics of the atmosphere, we do not have detailed profiles of the atmosphere structure at our sites, so we have varied only the cloud optical depths to minimize complications arising from the use of multiple adjustable parameters. We have ignored the potential effects of arctic haze, which would reduce the optical depths needed for comparing the models with observations.

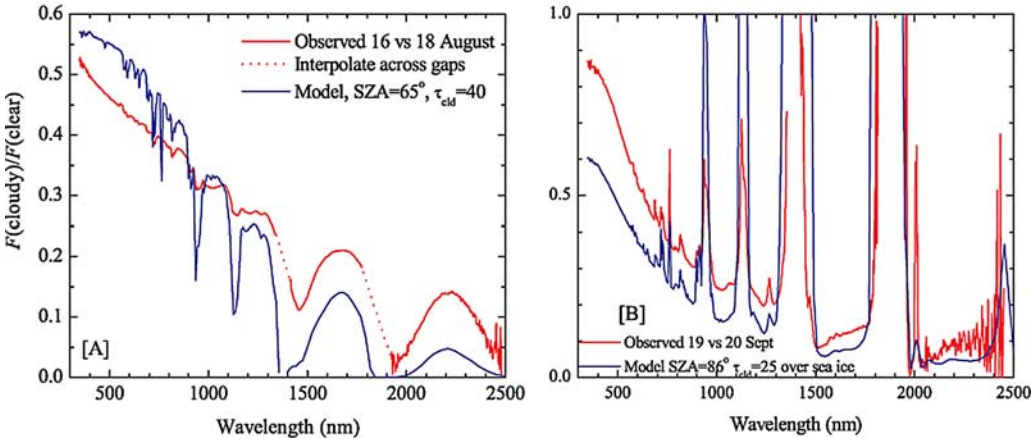

Figure 9. Ratio of incident irradiance spectra for cloudy to solar disk clearly visible cases for (a) high Sun (65°) and (b) low Sun (86°). Cloudy cases are for 18 August and 20 September. The red curves are observational results, and the blue curves show corresponding model comparisons based on SBDART calculations with a single cloud layer from 1000 to 5000 m elevation. The ordinate in Figure 9b has been set at 1.0. While both the observations and the model results show values above 1.0, these represent extremely low light levels and are ignored.

[25] The results of these comparisons are shown in Figure 8, and in general, the agreement is very good. The model results match the cloudy cases using cloud optical depths of 30, 15, and 10 for 22 August, 27 August, and 20 September, respectively. While corrections for actual atmospheric profiles of temperature, pressure, water vapor, and cloud particle size distributions and water versus ice content would be appropriate for a more precise match, we do not have the necessary data to justify such refinements at this point. There is generally good agreement in the location and intensity of the absorption bands as well as across the continuum. While a more detailed investigation is beyond the scope of the present study, the agreement seen here supports the precision of the spectral values and indicates that most of the spectral structure is due to real absorption features rather than observational noise.

[26] The comparison for 16–17 August shows that the model for clear-sky conditions with a solar zenith angle of 65° predicts significantly higher irradiance levels than the observations as plotted in Figure 8b. Since the weather wasn't fully clear anytime in August and the 16–17 August observations were the clearest conditions available during the first half of the experiment, we have assumed that a thin cloud layer was present. We obtain a good fit assuming an optical depth of 5 for that layer. We experienced clear conditions on 16 and 19 September, and the comparison for those cases is quite good (Figure 8b). We note that the broad absorption feature for low-Sun angle centered at about 600 nm in the observations is also present in the model results. This is due to the Chappuis absorption band of ozone, and its presence is accentuated due to flattening of the visible part of the spectrum by Rayleigh scattering.

7. Clear Versus Cloudy Skies

[27] The variation of the proportion of visible versus infrared irradiance has been identified as a significant variable. It changes with cloud concentration, weighting the integrals in equations (1), (2) and (3) more heavily at shorter wavelengths for cloudier conditions. To illustrate this effect, we show ratios of spectra for full overcast conditions to clear conditions for high (Figure 9a) and low (Figure 9b) Sun conditions (solar zenith angles of 65° and 86°, respectively). The case used for "clear sky" for high Sun is actually solar disk clearly visible (SDCV) from 16 to 17 August because in August the sky was never completely clear. Also shown are ratios from the corresponding cases calculated using SBDART. The introduction of a cloud layer increases the optical depth of the atmosphere with attenuation increasing steadily with wavelength due to the H_2O cloud particles. For the higher Sun (August), the ratios in Figure 9a show additional attenuation in the infrared water bands relative to the interband zones. This is the behavior we expected in general. The differences between observed and modeled values for the high-Sun case are probably due to variations in the atmospheric water vapor profiles for the cases compared.

[28] For 86°, the ratio in the continuum between the H_2O bands also decreases at longer wavelength, and the intensities in the absorption bands also decrease strongly; however, the intensity ratio within the bands is higher than in the interband zones, producing a series of sharp upward spikes. This holds both for the observations and for the model results. Although the observed ratio values at the top of these spikes are excessively noisy because of the low-intensity levels there, the models indicate that the clear-cloudy ratio can even exceed unity; that is, the downwelling irradiance in certain bands can be greater under cloudy conditions than for clear skies.

[29] This behavior is caused by a combination of the diffusing effect of the clouds on the incident beam and the concentration of the preponderance of the atmospheric water vapor in the layer between the clouds and the surface. This produces strong in-band absorption but almost no scattering. Under clear conditions for low Sun, the direct beam traverses the water vapor layer at a high zenith angle,

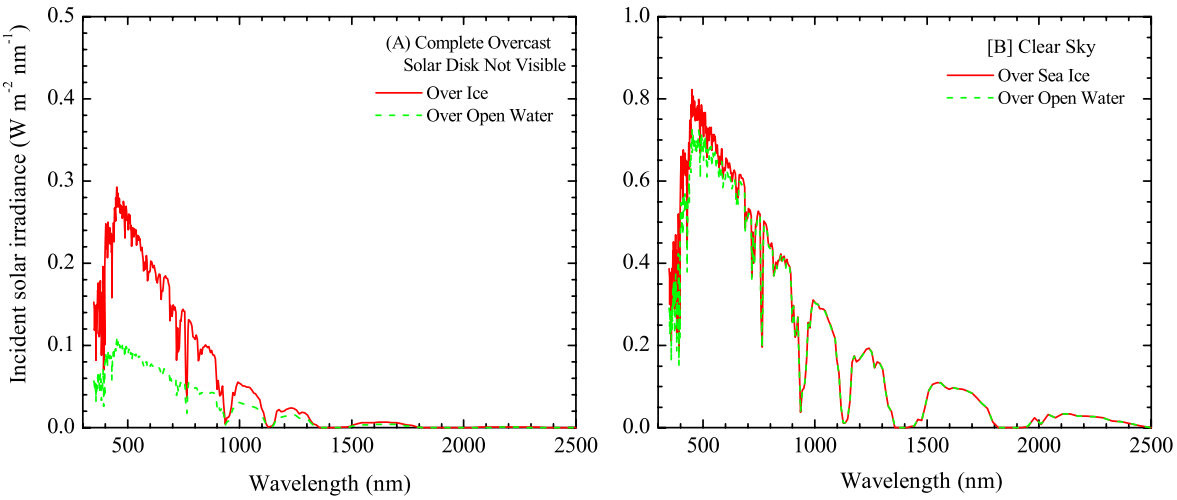

Figure 10. Model calculations of incident irradiance over surfaces with high and low albedos (sea ice and open water, respectively): (a) complete heavy overcast, with $\tau_{cld} = 30$ and solar zenith angle = 70°, and (b) clear sky, with solar zenith angle = 65°.

and the optical path length through the water vapor is very large. For cloudy conditions, the effective zenith angle is near 53° [e.g., *Wiscombe and Warren*, 1980], so the optical path length of the radiation through the water vapor layer is much lower and the resulting attenuation by the water vapor in the H_2O bands is much less, enough to offset the absorption produced by the cloud layer for the very low Sun cases producing the spikes observed. The continuum radiation interacts strongly with the cloud layer as it does for the higher-Sun case, but it is much less strongly affected by the underlying water vapor and the continuum ratio decreases in the infrared as for the higher-Sun case. At the core of the bands, the attenuation is sufficiently strong that the numerical limit of the computer is reached and the model assigns arbitrary very low values to the direct beam irradiance to avoid numerical instability. The values for these wavelength intervals have been removed from Figure 9b.

[30] For higher Sun angles, the change in effective path length caused by the cloud layer is sufficiently small that the additional attenuation by the clouds themselves in the bands relative to the continuum decreases the ratio in the H_2O bands. As a corollary, this behavior shows that the water vapor concentration within the clouds must have been very small in mid-September when the Sun was low and the atmosphere was colder.

8. Discussion

8.1. Effect of Surface Albedo

[31] Multiple backscatter of radiation from the surface and then downward by the atmosphere has a significant influence on $F_o(\lambda)$. These are the phenomena described as "water sky" and "ice blink" by early explorers, and the effects are still used by navigators as a means to identify the presence of a lead within the ice pack or the ice edge from open water, respectively. Because matched cases of readings over open water and continuous ice cover with the same solar zenith angle were not practical in general for our experiment, and because of the success in matching the model to observational results, we use results from SBDART to illustrate this effect. Comparative spectra for cloudy skies and for clear skies are shown in Figure 10. The contrast ratios of irradiance over water versus over sea ice [$CR_\lambda \equiv F_o(\lambda, \text{water})/F_o(\lambda, \text{sea ice})$] are shown in Figure 11 for clear and cloudy conditions. Including multiple reflections between the surface and the atmosphere and assuming diffuse reflection, the ratio is given to a good approximation using a conventional multiple reflection series representation via

$$CR_\lambda = \frac{[1 - \alpha_\lambda(\text{sea ice}) \cdot \alpha_\lambda(\text{atmos})]}{[1 - \alpha_\lambda(\text{water}) \cdot \alpha_\lambda(\text{atmos})]}, \quad (4)$$

where α_λ(atmos) is the spectral albedo of the cloud layer for upwelling radiation or of the clear atmosphere. The spectral albedo of water is low and almost independent of wavelength. Variations in CR_λ due to differences in surface albedo are much greater for the cloudy case because of the strong downward scattering by the clouds. A measurable effect, however, is also present for the clear-sky cases, primarily in the blue and UV spectral regions where Rayleigh scattering in the atmosphere is strongest. This is apparent in Figure 11. When the cloud albedo is small, across the solar infrared, the ratio is close to one. At short wavelengths, where the albedo of the ice increases strongly, the ratio decreases. For the clear-sky case, the ratio mirrors the increase in Rayleigh scattering. For the cloudy case, the ratio shows the combined effects of the cloud and surface albedos. The presence of haze would enhance the effect for "clear–sky" cases.

[32] Using equation (4), we can extract the albedo of the sky by itself. Results are shown for cases of clear skies in Figure 11b and cloudy skies in Figure 11a. For the clear-sky case, the strong increase toward shorter wavelengths again shows that the sky albedo is dominated by Rayleigh scattering. For the cloudy case, the continuum albedo is nearly independent of wavelength from 350 to 1000 nm and then decreases gradually between the strong H_2O vapor absorption bands, where the albedo is low.

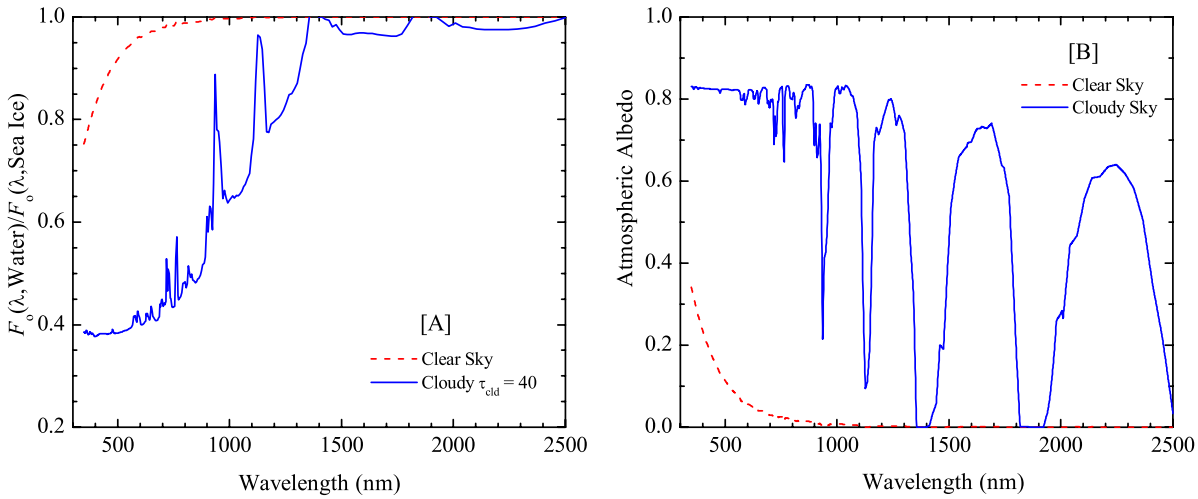

Figure 11. (a) Irradiance contrast ratios, $CR_\lambda = F_o(\lambda, \text{water})/F_o(\lambda, \text{sea ice})$, for water versus sea ice under clear and cloudy conditions illustrating the phenomenon of "water sky," darkening of the sky over an open water area in a field of sea ice. The inverse of CR_λ is called "ice blink." (b) Upward looking atmospheric spectral albedos derived from equation (4).

8.2. Wavelength Integrated Albedo

[33] To evaluate the effect of different sky conditions on total albedo, we have taken spectral albedo data for selected cases from *Perovich et al.* [2002] and *Grenfell and Perovich* [2004]. Using equation (1) to calculate α_{tot} under clear and cloudy skies for six representative Arctic surface types, we obtain the results shown in Table 1.

[34] The largest change in total albedo, $\delta\alpha_{tot}$, versus cloud conditions is an increase under a cloud cover of 0.05 and 0.08 relative to clear skies for solar zenith angles of 65° and 86°, respectively. The variation is approximately the same for cold Arctic snow and bare sea ice. Almost no change occurs over open water because the spectral albedo is nearly independent of wavelength. Over dry tundra, $\delta\alpha$ has the opposite sign and decreases under a cloud cover by 0.02 to 0.04 depending on solar zenith angle. Variations in the spectral shape between clear and cloudy conditions are significant and generally consistent with prior calculations [*Grenfell and Perovich*, 1984, 2004]. Previous values were calculated for representative values of $F_o(\lambda)$ for clear and complete overcast sky conditions for solar zenith angles near 65°, but with a less precise calibration. For corresponding cases, the results were quite similar to the present values.

[35] Analogous calculations for K_{tot} and I_o are also possible using equation (1); however, they require values of the irradiance within the ice. The spectral extinction coefficient of sea ice and snow are also strongly wavelength dependent and their magnitudes depend on the structure of the ice. So although $F_o(\lambda)$ values are central to the determination of K_{tot} and I_o, accurate calculation requires the use of a detailed radiative transfer code, and the results depend not only on the degree of cloudiness but also on the structure of the ice. This is beyond the scope of the present work, but the data required, and additional considerations for calculations of this sort are presented by *Grenfell et al.* [2006] and *Light et al.* [2008].

8.3. Comparison With Pyranometer Observations

[36] Eppley pyranometer observations of total incident shortwave radiation, F_o(Eppley), were recorded as 5-min averages continuously throughout the transect. Condensation was removed from the dome of the instrument on a regular basis as necessary. The results can be compared with the corresponding values of $F_o(\lambda)$ integrated numerically over the solar spectrum.

[37] When we included all cases in the comparison, we found a large amount of scatter and a bias such that the pyranometer results showed systematically higher values than the spectral data. Inspection of the record also showed that the pyranometer observations for cloudy conditions were rather noisy, particularly for thinner nonuniform cloud conditions. As a result, the spectrophotometer observations were often made selectively under momentary episodes of heavier, more uniform cloud conditions. This tended to produce a bias toward lower spectral irradiance levels during the 5-min averaging intervals for F_o(Eppley). To avoid this bias, we have restricted the comparison to cases where the solar disk was unobscured for which the short-term fluctuations in F_o were smallest. The results are shown in Figure 12.

[38] The precision in F_o(Eppley) was taken to be 3 W/m^2 based on the noise level of the voltage recorder. Shadowing corrections were included in full detail as mentioned above, and cases were excluded for which riming or water droplets on the pyranometer dome were reported. The error in F_o(integrated) was taken to be 5% based on the noise level of the standard lamp used for calibration as well as the uncertainties in the precision of the angular sensitivity of the cosine receptor and in the shadowing correction, which assumed that the diffuse radiation field was isotropic. The agreement between the two observation sets appears quite good; however, close examination of the low-light-level results suggests a slight residual bias. This may be due in part to the broader wavelength range of the pyranometer. In

Table 1. Integrated (Total) Albedos (α_{tot}) Versus Surface Type and Sky Conditions[a]

Sky Conditions	α_{tot}	Δ
Cold Arctic Snow		
Clear 65°	0.852	0.000
SDCV 65°	0.872	0.021
Cloudy 65°	0.906	0.055
Clear 86°	0.856	0.004
Cloudy 86°	0.931	0.079
Bare Sea Ice		
Clear 65°	0.601	0.000
SDCV 65°	0.619	0.018
Cloudy 65°	0.654	0.053
Clear 86°	0.603	0.002
Cloudy 86°	0.687	0.085
Early Melt Pond		
Clear 65°	0.227	0.000
SDCV 65°	0.234	0.007
Cloudy 65°	0.255	0.028
Clear 86°	0.221	−0.006
Cloudy 86°	0.285	0.058
Late Melt Pond		
Clear 65°	0.125	0.000
SDCV 65°	0.128	0.004
Cloudy 65°	0.136	0.012
Clear 86°	0.122	−0.002
Cloudy 86°	0.146	0.021
Open Water		
Clear 65°	0.0701	0.000
SDCV 65°	0.0704	0.001
Cloudy 65°	0.0719	0.002
Clear 86°	0.0697	0.000
Cloudy 86°	0.0736	0.004
Dry Tundra		
Clear 65°	0.178	0.000
SDCV 65°	0.174	−0.004
Cloudy 65°	0.158	−0.021
Clear 86°	0.183	0.005
Cloudy 86°	0.133	−0.045

[a]Conditions are degree of cloudiness and solar zenith angle. Δ is the difference between the listed value and clear-sky conditions at 65° solar zenith angle. Spectral albedos for each surface type are assumed to be the same for all illumination conditions. SDVC is solar disk clearly visible.

view of the sensitivity of the comparison to the precise timing of the observations, however, we have not introduced more detailed corrections to attempt to account for the residual. Although this reflects possible uncertainty in F_o, the most important aspect for calculations of α_{tot}, K_{tot} and I_o, equations (1) to (3), for example, is the shape of the spectrum, which we believe is accurately represented here.

8.4. Cloud Optical Depth

[39] The cloud optical depths from the present comparison of model results and observations must be regarded as a fitting parameter at this stage due to uncertainty and variation in the actual optical properties of the atmosphere during the transect. Cloud optical depth depends strongly on both total water/ice content and effective cloud particle diameter. It also depends on the relative amounts of solid to liquid phase particles, all of which vary considerably in space and time across the Arctic. Derived values would also need to account for effects of arctic haze, not considered in the present analysis. So a more precise determination of τ_{cld} is not practical with the present data set. The values we find, for cloud optical depths in the range 10 to 30 for fully overcast Arctic stratus, are consistent with previous observations [*Hahn et al.*, 2001; *Herman and Curry*, 1984; *Tsay and Jayaweera*, 1984; *Marshunova and Mishin*, 1994; *Alexandrov et al.*, 2004].

[40] The equivalent liquid or ice water path (*LWP*) (g/m^2) can be related to the cloud optical depth in terms of equivalent spheres via the following equation [e.g., *Grenfell and Warren*, 1999; *Neshyba et al.*, 2003]:

$$\tau_{cld} = \frac{3}{4} \cdot \frac{LWP \cdot Q_{ext}}{r_{sph} \cdot \rho_{sph}}, \quad (5)$$

where r_{sph} is the effective radius of the cloud particles, ρ_{sph} is the density of the cloud particles, and Q_{ext} is the single scattering extinction coefficient. For August, we take τ_{max} = 30 and assume the particles were water drops with radii in the range 3–7 μm [*Herman and Curry*, 1984]. For mid to late September, we have τ_{max} = 10, and the model was applied assuming the cloud particles were liquid droplets in this case as well since 10-m air temperatures were still near −10°C at that time. The resulting maximum *LWP* values fell in the range 60–140 g/m^2 for the August observations and 20–47 g/m^2 for September, also consistent with the previous results cited above.

9. Conclusions

[41] Improved values of $F_o(\lambda)$ are presented for various solar elevations and cloud conditions during the late Summer and early Fall across the Arctic Basin. The spectral shape is of central importance for the wavelength-integrated quantities α_{tot}, K_{tot} and I_o commonly used in conjunction with shortwave radiometric observations and regional radiative energy balance modeling. This formulation is useful because it requires only the spectral shape of the irradiance,

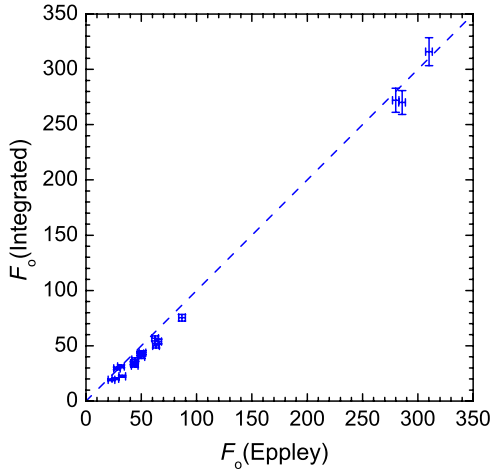

Figure 12. Comparison of F_o (ASD) = $\int_{SW} F_o(\lambda)\, d(\lambda)$ with F_o(pyranometer) for cases where the solar disk was unobscured. The dashed line indicates one-to-one agreement.

which is much more robust than the precise values of the absolute calibration, and it provides the parameters needed to interpret routinely measured integrated shortwave irradiance values.

[42] More general radiative transfer analysis uses $F_o(\lambda)$ directly, and we find that both the relative and absolute magnitudes of $F_o(\lambda)$ are consistent with a detailed model in which only a single parameter, the cloud optical depth, is not directly specified a priori. The spectra are also consistent in shape and magnitude with recent results from the Arctic and Antarctic sea ice zones. Certain unusual spectral features, the strong attenuation around the Chappuis ozone band and the enhancement of radiation in the strong H_2O absorption bands by a cloud cover at very large solar zenith angles compared to clear-sky conditions, are confirmed and explained by the model analysis. Absolute values of $F_\lambda(\theta_o)$ are compared with concurrent pyranometer observations and are consistent to within about 5%.

[43] To represent the continuum radiation, which accounts for almost all of the incident solar radiative energy, we applied a supervised principal component analysis. Three principal components were sufficient to explain over 99% of the variance in the data set. *PC*1 explains primarily the general attenuation at all continuum wavelengths, and *PC*2 explains the bulk of the increased absorption due to H_2O in the infrared. *PC*3 explains the residual contribution from Rayleigh scattering and accentuation of the Chappuis ozone band but may also contain a contribution from observational noise.

[44] New values of total (wavelength integrated) albedo are presented. For a particular surface type, they vary by as much as 10% between clear and complete overcast conditions due primarily to selective absorption by water in the solar infrared. The effects of multiple reflection between clouds and the surface are demonstrated, providing quantitative estimates for the phenomena of "ice blink" and "water sky."

[45] Cloud optical depths up to 30 at a wavelength of 550 nm were required to explain the observations of complete overcast in August, a month with essentially no clear-sky days in the vicinity of the ship. Lower values ($\sim$10) were needed in September, consistent with the clearer skies and colder atmosphere present at the time. Additional details on the project as well as the full radiation data set are available on our web site: http://www.arcticice.org/hotraxweb/.

[46] **Acknowledgments.** We thank Bruce Elder and Jeremy Harbeck for invaluable assistance with the field observations. We also wish to thank Steve Hudson, Bonnie Light, and Steve Warren for incisive comments on the manuscript. Steve Hudson also provided a copy of the SBDART code and critical help in implementing it. Funding for the field experiment provided by the National Science Foundation under grant ARC 0454900 is gratefully acknowledged.

References

Alexandrov, E. I., N. N. Bryazgin, A. A. Dement'ev, and V. F. Radionov (2004), Meteorological Regime of the Arctic Basin *(Метеролоический РеНсим Арктическоо БассейНа)*, vol. II, *Климат приледНосо слоя атмосфуры Арктическоо бассейНа* (*Climate of the Near-Surface Layers of the Atmosphere in the Arctic Basin*), edited by G. V. Alexeyev, Hydrometerol. Publ., St. Petersburg, Russia.

Brandt, R. E., and S. G. Warren (1993), Solar-heating rates and temperatures profiles in Antarctic snow and ice, *J. Glaciol.*, *39*, 99–110.

Briegleb, B. P., and B. Light (2007), A Delta-Eddington multiple scattering parameterization for solar radiation in the sea ice component of the community climate system model, *Tech. Note TN-472+STR*, 108 pp., Natl. Cent. for Atmos. Res., Boulder, Colo.

Curry, J. A., J. L. Schramm, and E. E. Ebert (1995), On the sea ice albedo climate feedback mechanism, *J. Clim.*, *8*, 240–247, doi:10.1175/1520-0442[1995]008<0240:SIACFM>2.0.CO;2.

Curry, J. A., J. L. Schramm, D. K. Perovich, and J. O. Pinto (2001), Applications of SHEBA/FIRE data to evaluation of snow/ice albedo parameterizations, *J. Geophys. Res.*, *106*(D14), 15,345–15,355, doi:10.1029/2000JD900311.

Gast, P. R. (1960), Solar radiation, in *Handbook of Geophysics*, edited by C. F. Campen, pp. 16-14–16-32, Macmillan, New York.

Grenfell, T. C. (1991), A radiative transfer model for sea ice with vertical structure variations, *J. Geophys. Res.*, *96*(C9), 16,991–17,001, doi:10.1029/91JC01595.

Grenfell, T. C., and G. A. Maykut (1977), The optical properties of ice and snow in the Arctic Basin, *J. Glaciol.*, *18*, 445–463.

Grenfell, T. C., and D. K. Perovich (1981), Radiation absorption coefficients of polycrystalline ice from 400 to 1400 nm, *J. Geophys. Res.*, *86*, 7447–7450, doi:10.1029/JC086iC08p07447.

Grenfell, T. C., and D. K. Perovich (1984), Spectral albedos of sea ice and incident solar irradiance in the southern Beaufort Sea, *J. Geophys. Res.*, *89*, 3573–3580, doi:10.1029/JC089iC03p03573.

Grenfell, T. C., and D. K. Perovich (2004), The seasonal and spatial evolution of albedo in a snow-ice-land-ocean environment, *J. Geophys. Res.*, *109*(C1), C01001, doi:10.1029/2003JC001866.

Grenfell, T. C., and S. G. Warren (1999), Representation of a nonspherical ice particle by a collection of independent spheres for scattering and absorption of radiation, *J. Geophys. Res.*, *104*, 31,697–31,709, doi:10.1029/1999JD900496.

Grenfell, T. C., B. Light, and D. K. Perovich (2006), Spectral transmission and implications for the partitioning of shortwave radiation in Arctic sea ice, *Ann. Glaciol.*, *44*, 1–6, doi:10.3189/172756406781811763.

Hahn, C. J., W. B. Rossow, and S. G. Warren (2001), ISCCP cloud properties associated with standard cloud types identified in individual surface observations, *J. Clim.*, *14*, 11–28, doi:10.1175/1520-0442[2001]014<0011:ICPAWS>2.0.CO;2.

Herman, G. F., and J. A. Curry (1984), Observational and theoretical studies of solar radiation in Arctic stratus clouds, *J. Clim. Appl. Meteorol.*, *23*, 5–24, doi:10.1175/1520-0450[1984]023<0005:OATSOS>2.0.CO;2.

Holland, M. M., and C. M. Bitz (2003), Polar amplification of climate change in coupled models, *Clim. Dyn.*, *21*, 221–232, doi:10.1007/s00382-003-0332-6.

Holland, M. M., C. M. Bitz, E. C. Hunke, W. T. Lipscombe, and J. L. Schramm (2006), Influence of the sea ice thickness distribution on polar climate in CCSM3, *J. Clim.*, *19*, 2398–2414, doi:10.1175/JCLI3751.1.

Light, B., T. C. Grenfell, and D. K. Perovich (2008), Transmission and absorption of solar radiation by Arctic sea ice during the melt season, *J. Geophys. Res.*, *113*, C03023, doi:10.1029/2006JC003977.

Marshunova, M. S., and A. A. Mishin (1994), *Handbook of the Radiation Regime of the Arctic Basin* (*Results From the Drift Stations*) (in Russian), edited by V. F. Radionov, Gidrometeoizdat, Saint Petersburg, Russia. (English translation, *Tech. Rep. 9413*, Appl. Phys. Lab., Univ. of Wash., Seattle 1994.).

Neshyba, S. P., T. C. Grenfell, and S. G. Warren (2003), Representation of a nonspherical ice particle by a collection of independent spheres for scattering and absorption of radiation: 2. Hexagonal columns and plates, *J. Geophys. Res.*, *108*(D15), 4448, doi:10.1029/2002JD003302.

Perovich, D. K., and J. W. Govoni (1991), Absorption coefficients of ice from 250 to 400 nm, *Geophys. Res. Lett.*, *18*, 1233–1235, doi:10.1029/91GL01642.

Perovich, D. K., T. C. Grenfell, B. Light, and P. V. Hobbs (2002), Seasonal evolution of multiyear Arctic Sea ice, *J. Geophys. Res.*, *107*(C10), 8044, doi:10.1029/2000JC000438.

Rabbette, M., and P. Pilewskie (2002), Principal component analysis of Arctic solar irradiance spectra, *J. Geophys. Res.*, *107*(C10), 8049, doi:10.1029/2000JC000566.

Radionov, V. F., N. N. Bryazgin, and Y. I. Aleksandrov (1996), *The Snow Cover of the Arctic Basin* (in Russian), 102 pp., Gidrometeoizdat, St. Petersburg, Russia. (English translation *Tech. Rep. APL-UW TR 9701,* Polar Sci. Cent., Univ. of Wash., Seattle, 1996).

Ricchiazzi, P., S. Yang, C. Gautier, and D. Sowle (1998), SBDART: A research and teaching software tool for plane-parallel radiative transfer in the Earth's atmosphere, *Bull. Am. Meteorol. Soc.*, *79*(10), 2101–2114, doi:10.1175/1520-0477[1998]079<2101:SARATS>2.0.CO;2.

Sauberer, F. (1950), Die spektrale Strahlungsdurchlässigkeit des Eises (The spectral transmissivity of ice), *Wetter Leben*, *2*, 193–197.

Sauberer, F., and Dirmhirn (1958), Das Strahlungsklima (Radiation climatology), in *Klimatographie von Österreich* (*Climatography of Austria*), vol. 3, 1st ed., edited by F. Steinhauser, O. Eckel, and F. Lauscher, pp. 13–102, Österreich. Akad. der Wiss., Vienna.

Tsay, S.-C., and K. Jayaweera (1984), Physical characteristics of Arctic clouds, *J. Clim. Appl. Meteorol.*, *23*, 584–596, doi:10.1175/1520-0450[1984]023<0584:PCOASC>2.0.CO;2.

Warren, S. G. (1984), Optical constants of ice from the ultraviolet to the microwave, *Appl. Opt.*, *23*, 1206–1225.

Warren, S. G., R. E. Brandt, and T. C. Grenfell (2006), Visible and near-ultraviolet absorption spectrum of ice from transmission of solar radiation into snow, *Appl. Opt.*, *45*(21), 5320–5334, doi:10.1364/AO.45.005320.

Warren, S. G., R. M. Eastman, and C. J. Hahn (2007), A survey of changes in cloud cover and cloud types over land from surface observations, *J. Clim.*, *20*, 717–738, doi:10.1175/JCLI4031.1.

Wiscombe, W. J., and S. G. Warren (1980), A model for the spectral albedo of snow. I: Pure snow, *J. Atmos. Sci.*, *37*(12), 2712–2733.

T. C. Grenfell, Department of Atmospheric Sciences, Box 351640, University of Washington, Seattle, WA 98195, USA. (tcg@atmos.washington.edu)

D. K. Perovich, ERDC-CRREL, 72 Lyme Road, Hanover, NH 03755, USA. (donald.k.perovich@usace.army.mil)